CHAPTER- 4

Effects of Different CeO_2 Morphologies for NO Reduction Using NH_3-SCR

Abstract

Ceria (CeO_2) offers several advantages in NH_3-SCR applications, which make it a promising catalyst for reducing nitrogen oxide (NO_x) emissions. Some key benefits include: Ceria holds a high oxygen storage capacity, readily storing and releasing oxygen during the SCR process. This property helps maintain a balanced and controlled oxygen environment, crucial for efficient SCR reactions. Ceria contains oxygen vacancies and defects in its crystal structure. These vacancies act as active sites for adsorbing and activating NH_3 molecules. As a result, ceria can effectively facilitate the adsorption and conversion of NH_3 to reactive nitrogen species that can reduce NO_x. Ceria exhibits excellent redox properties, enabling it to switch between Ce^{4+} and Ce^{3+} states during the SCR reaction. This redox ability plays a vital role in the catalytic process, enhancing the conversion of NO_x into harmless nitrogen and water. Pure ceria may have limitations at low temperatures. It can exhibit improved catalytic activity at lower operating temperatures when modified or combined with other active components. This is essential for effectively reducing NO_x emissions in low-temperature SCR applications. Ceria is known for its exceptional thermal stability, making it suitable for use in high-temperature environments, such as power plant flue gases. The stability of the catalyst ensures long-term performance and durability under challenging conditions. Unlike some other SCR catalysts, ceria has good water tolerance, meaning it can maintain its catalytic activity even in the presence of water vapor, which is common in flue gases. Ceria is environmentally friendly due to its natural abundance and low toxicity compared to other metal-based catalysts. It poses

minimal risks to human health and the environment. In general, pure CeO_2 exhibits poor activity for NH_3-SCR. The properties of these materials can be enhanced by changing their preparation conditions, using cerium precursors, and improving their morphologies. [1-5]

The present work successfully synthesized a series of CeO_2 with different morphologies. These catalysts were examined using BET, XRD, XPS, TEM, SEM-EDX, and Raman spectroscopy. Furthermore, these were used to evaluate the catalytic activity using NH_3 as reductant.

4.1. EXPERIMENTAL

4.1.1. Materials and methods

The commercially available chemicals and gases have been used in the tests without further purification. The chemicals and reagents utilized were sodium hydroxide (NaOH, 98% purity Chemika-biochemical-reagents), cerium (III) nitrate hexahydrate ($Ce(NO_3)_36H_2O$, 99.0% purity, SRL Pvt. Ltd.), and ethanol (99% purity, SD Fine-Chemical Limited). Deionized water was utilised to form aqueous solutions. The gases NH_3 (1000 ppm, Ar balanced), NO (1000 ppm, Ar balanced), O_2 (6 vol%, Ar balanced), and N_2 (99.99%) have been used for catalytic activity analysis.

4.1.2. Catalysts synthesis

Three different ceria morphologies (nano-rods, nano-cubes, and nano-polyhedral) were synthesized using the hydrothermal method, shows in the **Fig. 4.1**. In this process, an aqueous solution containing $Ce(NO_3)_3 \cdot 6H_2O$ was combined with a solution of the precipitant agent, NaOH, and mixed continuously at room temperature for uniform solution. The obtained mixtures were next placed into 100 ml Teflon-lined autoclaves to complete the hydrothermal process. The reaction temperature and time were then changed based on the desired morphologies of CeO_2, which is given in **Table 4.1**. The resulting precipitates were cooled to room temperature after the hydrothermal process, and ethanol and deionized water were then

used for washing to remove any potential ionic impurities. The subsequent precipitate was dried overnight at 65°C before being calcined for 4h at 500°C. The resultant samples were denoted by CeO_2-NR, CeO_2-NC, and CeO_2-NP for CeO_2-Nanorod, CeO_2-Nanocube, and CeO_2-Nanopolyhedral, respectively, in the manuscript.

Fig. 4.1. Flow diagram of catalysts synthesis

Table 4.1. Condition for different CeO_2 morphologies

Morphology	**Cerium nitrate (mole)**	**C_{NaOH} (mole)**	**Temperature (°C)**	**Time (h)**
CeO_2-NR	5	7	100	12
CeO_2-NC	5	15	180	24
CeO_2-NP	4.5	8.5	180	24

4.1.3. Characterization

The BET surface area and pore distribution were measured using the N_2 adsorption and desorption method using Micromeritics ASAP 2020. The samples have been degassed for 4h at 350°C.

The X-ray diffraction pattern was captured using a Rigaku Miniflex 600 X-ray Diffraction System for the phase identification of catalysts. Cu Kα radiation with a wavelength of 0.154 nm was employed, and the system was operated at 100 mA and 40 kV. The scanning process spanned from 5 to 100° (2θ) at a rate of 5° per minute. The International Centre for Diffraction Data (ICDD) was used to determine the crystalline phases. Additionally, the Scherrer equation was used to calculate crystal size.

The XPS was anaylzed using the AMICUS and Kratos Analytical instruments. Al-Ka radiation with an energy of 1486.7 eV was utilized for the investigation. The binding energy of the C 1s peak at 284.8 eV was used as a reference to calibrate the binding energies of O 1s, Pt 4f, and Ce 3d. The "origin" software was employed to anaylzed the obtained spectra, and Gaussian functions were utilized to fit the spectra.

The TECNAI 20G system was used to capture images as transmission electron microscopy (TEM) analysis was performed on porosity structure and arrangement.

The morphological properties of the synthesized samples were anaylzed using the SEM EVO 18-20-45 system, and gold sputtering was performed to reduce the charging effect.

A Renishaw sensor device with a 532 nm operating wavelength was used to evaluate the catalysts using Raman spectroscopy. Between 100 and 2000 cm^{-1}, there was a Raman shift.

4.1.4. Catalytic performance

The setup for NO reduction, as shown in **Fig. 4.2**, comprised a series of gas lines. The reactor was also equipped with a heater and a controller to maintain temperature. The output line included a condenser for water condensation and a gas-liquid separator to separate water vapor. To prevent condensation of H_2O before entering the reactor, the pre-heater line temperature was maintained above 90°C. A programmable temperature controller connected to an internal thermocouple controlled the reaction conditions. The gas flow rates were carefully controlled using a mass flow controller. To determine the NO gas content in both the input and output, chemiluminescence analysis was performed using a specialized instrument from UNIPHOS ENVIROTRONIC Pvt. Ltd., based in India. **Equations (1)**, **(2)**, **(3)**, and **(4)** were used to calculate the NO conversion, N_2 selectivity, reaction rate, and turn over frequency (TOF) respectively.

$$\text{NO conversion (\%)} = \left(\frac{NO_{in} - NO_{out}}{NO_{out}}\right) \times 100\% \quad (4.1)$$

$$N_2 \text{ selectivity (\%)} = \left(\frac{N_2}{NO_{in} - NO_{out}}\right) \times 100\% \quad (4.2)$$

$$\text{Reaction rate [mol.g}^{-1}\text{cats}^{-1}\text{]} = \frac{X_{NO}[\%] X F_{NO_X}[L min^{-1}]}{60 X [s min^{-1}] X 22.4 [L min^{-1}] X M_{cat}[g]} \quad (4.3)$$

$$\text{TOF [s}^{-1}\text{]} = \frac{F_{NO}\,[L\,min^{-1}] \times NO_{Conversion}\,[\%]}{m[g] \times H_{2\,Consumption}\,[mol\,g^{-1}] \times 2 \times 22.4\,[L\,mol^{-1}] \times 60\,[s\,min^{-1}]} \quad (4.4)$$

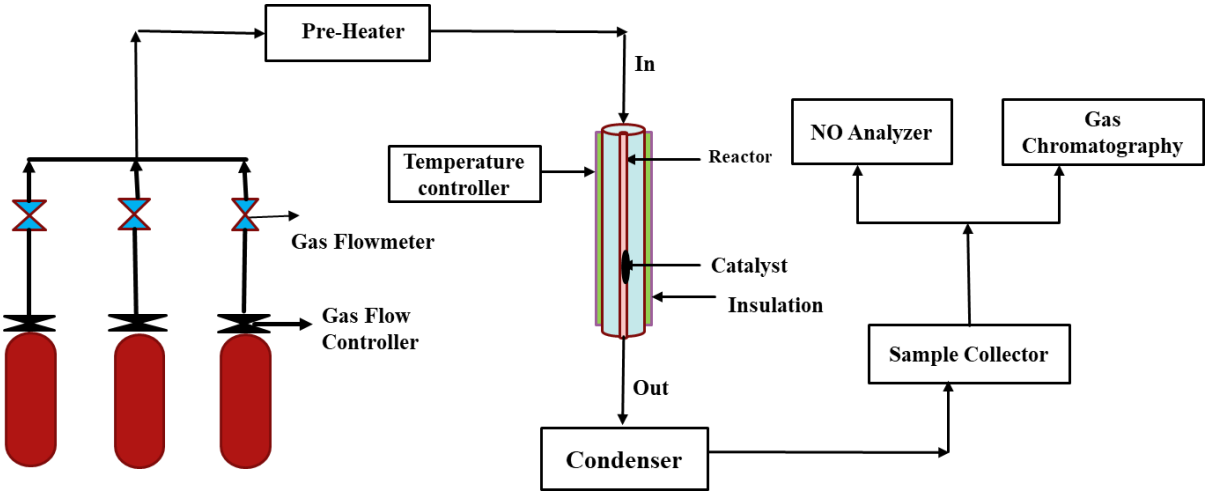

Fig. 4.2. Experimental setup

4.2. Results and discussion

4.2.1. Brunauer–Emmett–Teller (BET)

The physical properties of different morphologies of CeO_2 were assessed using the Brunauer-Emmett-Teller (BET) method. The BET surface area, pore volume, and pore size of various morphologies, namely CeO_2-NR, CeO_2-NC, and CeO_2-NP, are presented in **Table 4.2**. All the supports exhibited Type IV isotherms, according to the IUPAC classification (**Fig. 4.3)**. Based on the BET data, the surface areas of the catalysts are as follows: CeO_2-NR (22.75 m^2-g^{-1})> CeO_2-NC (20.24 m^2-g^{-1}) > CeO_2-NP (18.98 m^2-g^{-1}). These values provide valuable insights into the specific surface areas of the supports which are crucial in understanding their potential for catalytic applications.

Table 4.2. Textural properties of CeO_2 support

Sample	S_{BET} (m^2-g^{-1})	Pore volume (cm^3-g^{-1})	Pore size (nm)
CeO_2-NR	22.75	0.11	12.23
CeO_2-NC	20.24	0.10	9.13
CeO_2- NP	18.98	0.09	9.57

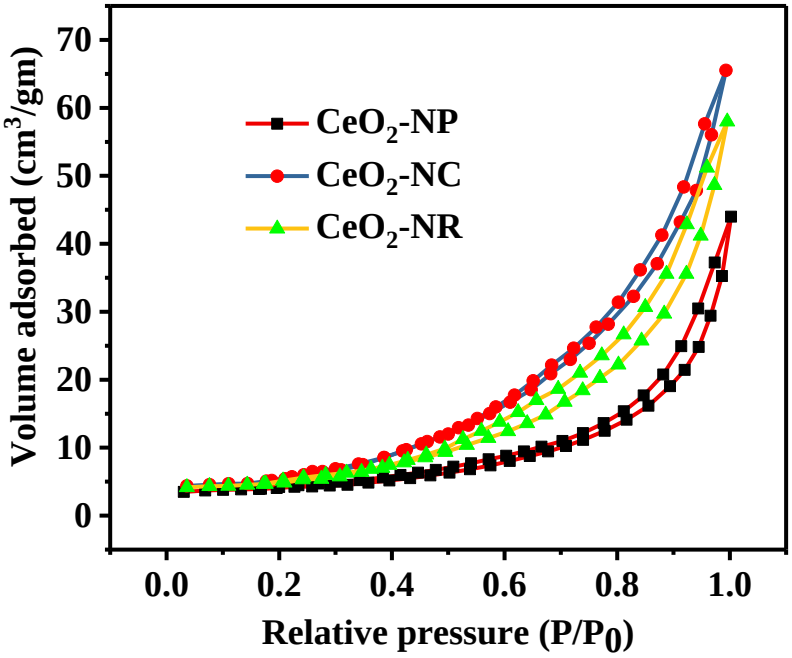

Fig. 4.3. N_2 adsorption and desorption isotherms of CeO_2-NR, CeO_2-NC, and CeO_2-NP

4.2.2. X-Ray Diffraction Analysis (XRD)

The X-ray diffraction (XRD) technique was used to anaylzed the phase structure of the samples. **Fig. 4.4** shows the XRD patterns of the synthesized samples: CeO_2-NR, CeO_2-NC, and CeO_2-NP. The observed diffraction peaks at 28.29, 32.96, 47.24, 55.12, 59.16, 69.23, 76.26, and 78.80 correspond to the crystal planes (111), (200), (220), (311), (222), (400), (331), and (420) of the face centered cubic (FCC) structure of ceria (JCPDS-81-0792). These peaks indicate that all the samples possess a crystalline nature.

The average crystal size of the samples was calculated using the Scherrer equation and the results are shown in **Table 4.3**. Among the CeO_2 morphologies studied, CeO_2-NR exhibited the smallest crystal size, while CeO_2-P had the largest crystal size. The crystal sizes of the CeO_2 morphologies can be ordered as follows: CeO_2-NR > CeO_2-NC > CeO_2-NP. The lattice parameters were calculated and are summarized in **Table 4.3**, which are very close to each other.

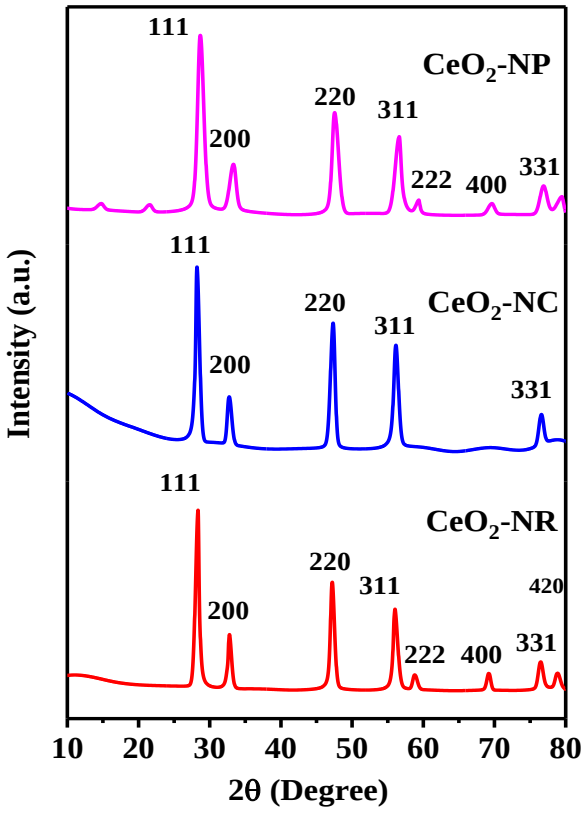

Fig. 4.4. XRD pattern of the samples

Table 4.3. Structural properties of different ceria morphology

Support	Lattice parameter (Å)	Average crystal size (nm)[a]	Lattice Strain ((Δd/d) [b]	Average particle size (nm)[c]
CeO_2-NR	5.41	12.2	0.018	45.8
CeO_2-NC	5.41	14.1	0.017	63.0
CeO_2-NP	5.42	14.5	0.017	37.5

[a] *Calculated by Scherrer equation [$d=k\lambda/\beta Cos\theta$, where d is crystalline, k is dimensionless shape factor, β is the line broadening at half the maximum intensity (FWHM),* and θ *is the Bragg angle]*

[b] *Calculated by Williamson–Hall equation[$\beta cos\theta=(k\lambda/d)+4\varepsilon sin\theta$, where is the lattice strain]*

[c] *Calculated from TEM image data*

4.2.3. X-ray Photoelectron Spectroscopy (XPS)

X-ray photoelectron spectroscopy (XPS) was used to analyze the chemical state and surface composition of CeO_2 structure. The spectrum of Ce 3d and O 1s investigation is shown in **Fig. 4.5** and **Fig. 4.6** respectively.

Fig. 4.5 showed the Ce 3d XPS spectra of different morphology of ceria. All ceria samples spectra were deconvoluted into six peaks with the letters u°, u^{i}, u^{ii}, v°, v^{i}, and v^{ii}. The series of the spin-orbit doublet peak, which is denoted by the letters u and v, respectively, indicates the Ce $3d_{3/2}$ and Ce $3d_{5/2}$ states. The Ce^{3+} ions peaks are u° (899.88 eV) and v° (881.63 eV), whereas the Ce^{4+} ions species are u^{i} (906.30 eV), u^{ii} (915.91 eV), v^{i} (887.65 eV), and v^{ii} (897.67 eV). The deconvoluted split peaks demonstrate that Ce^{3+} and Ce^{4+} ions are present in the CeO_2 oxides. The concentrations of surface ions and lattice oxygen in Ce^{3+} had a significant impact on the performance of the catalyst [6,7]. The formula for calculating the Ce^{3+} state's percentage evaluation is $[Ce^{3+}/(Ce^{3+}+Ce^{4+})]x100$. The data in **Table. 4.4** shows that CeO_2-NR had the greatest Ce^{3+} concentration among all the morphologies.

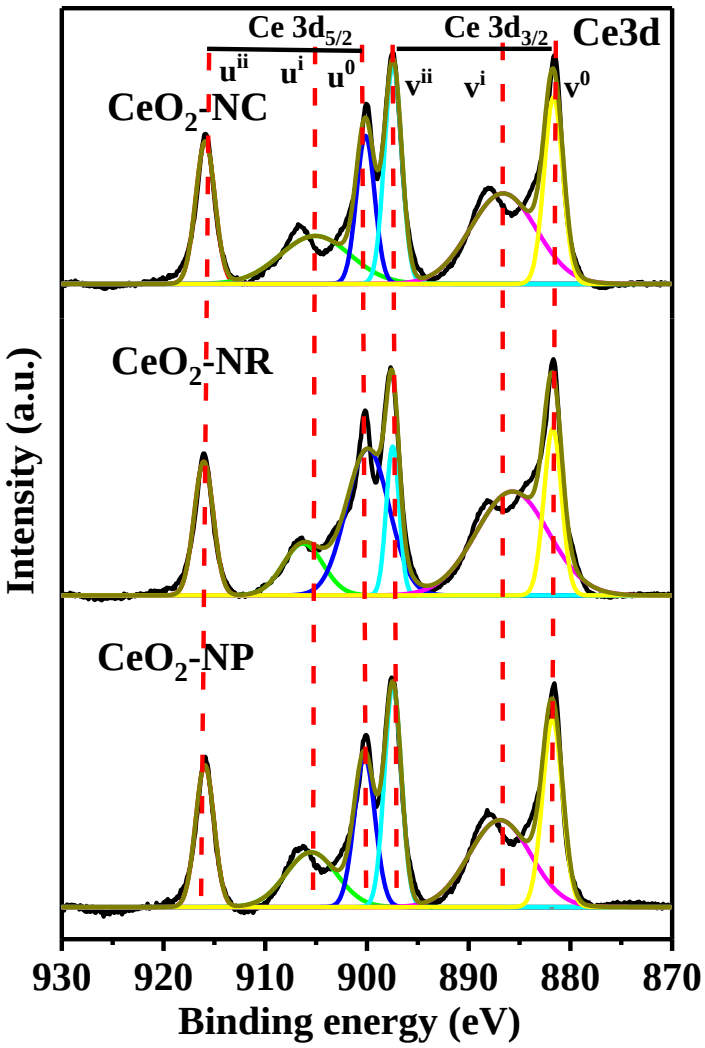

Fig.4.5. Ce 3d XPS graph of the catalysts

The de-convoluted O1s spectra of CeO_2 supports illustrate two peaks at 530 eV and 531.2 eV, shown in the **Fig. 4.6**. The peak at 530 eV can be attributed to lattice oxygen (O_α) whereas peak at 531.2 eV can be assigned to oxygen vacancies (O_β). The ratio can be used to evaluate the concentration of oxygen vacancies. [8,9] The ratio ranks in the following order: CeO_2-NR > CeO_2-NC > CeO_2-NP, given in the **Table 4.4**.

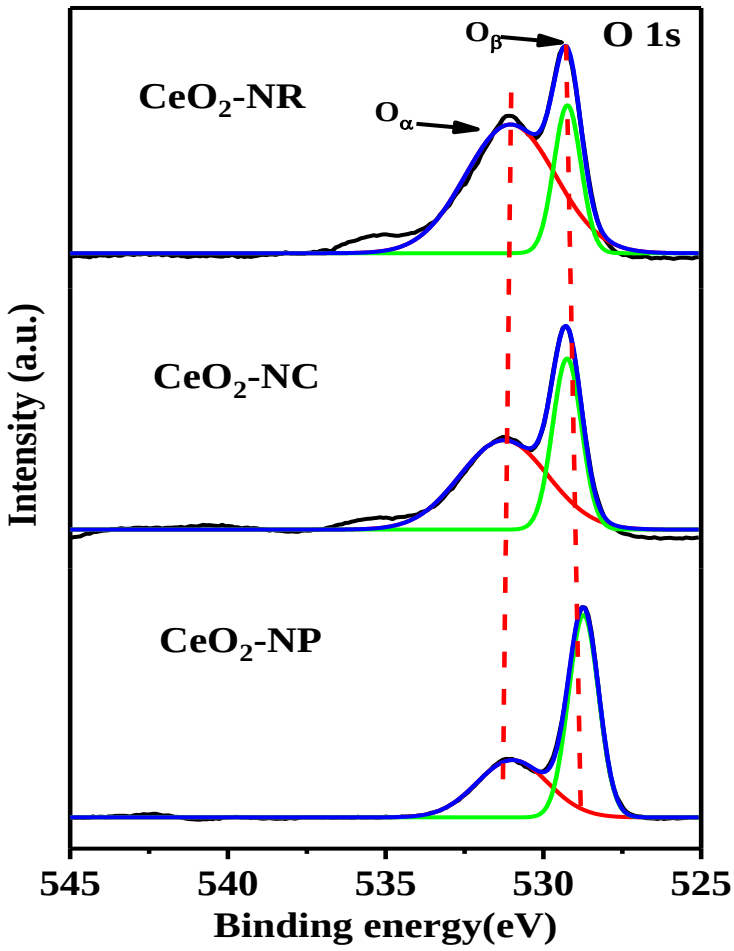

Fig. 4.6. O 1S XPS graph of the catalysts

Table 4.4. XPS results of Ce 3d and O1s for the catalysts

Catalysts	$(\frac{Ce^{3+}}{Ce^{3+}+Ce^{4+}})$	$(\frac{O_\alpha}{O_\alpha+O_\beta})$
CeO_2-NR	0.44	0.53
CeO_2-NC	0.43	0.50
CeO_2-NP	0.41	0.41

4.2.4. Transmission Electron Microscopy (TEM)

The TEM micrographs of CeO_2 in **Fig. 4.7** demonstrated that supports with rod, cube and polyhedral were successfully synthesized. Moreover, the TEM analysis revealed that the average particle size measured 37.5 nm, 63 nm, and 45.85 nm for the CeO_2-NP, CeO_2-NC, and CeO_2-NR, respectively. Particle size distribution can be understood by examining this information. **Fig. 4.7** includes Selected Area Electron Diffraction (SAED) patterns that display distinct rings. According to these patterns, all synthesized samples are crystalline, correlating with X-ray Diffraction (XRD) results.

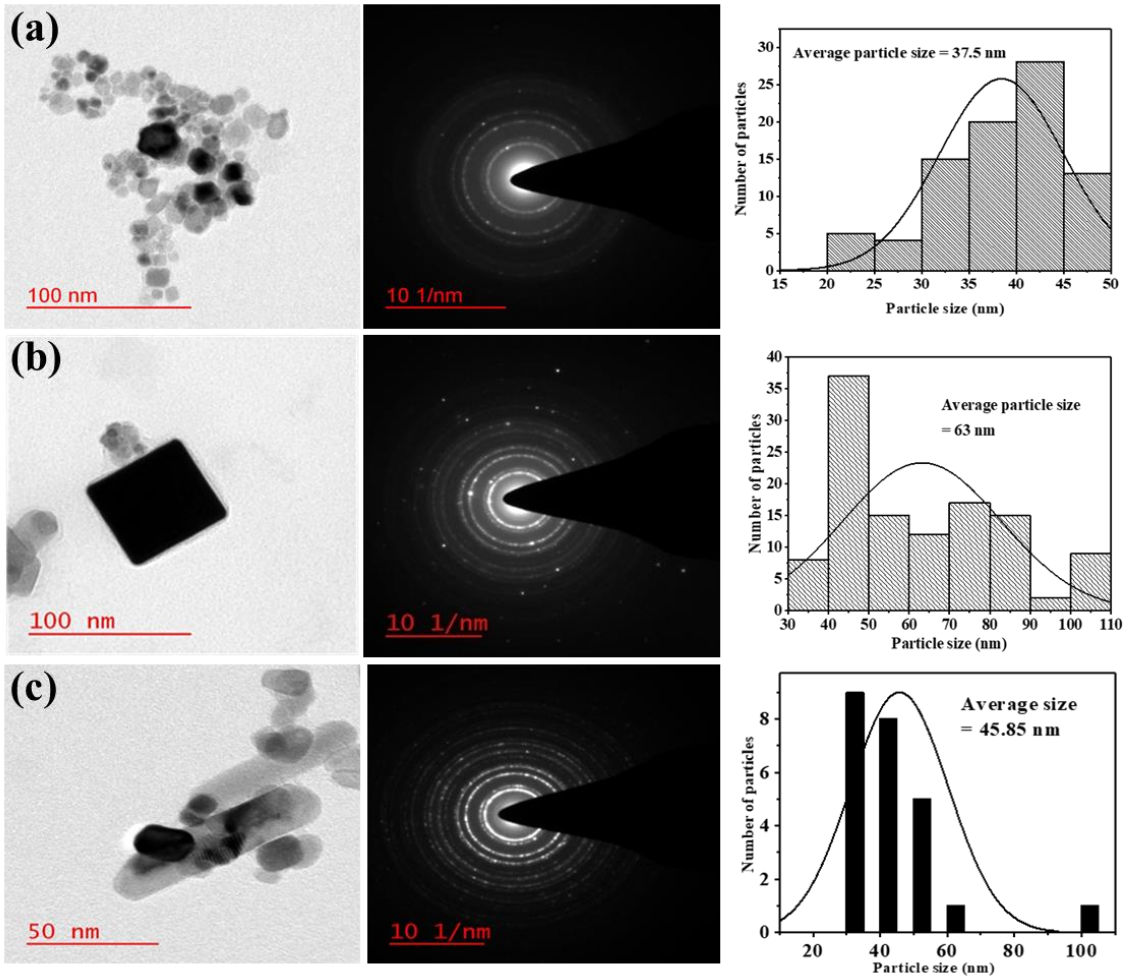

Fig. 4.7. TEM images of the samples: (a) CeO_2- NP, (b) CeO_2-NC, and (c) CeO_2-NR

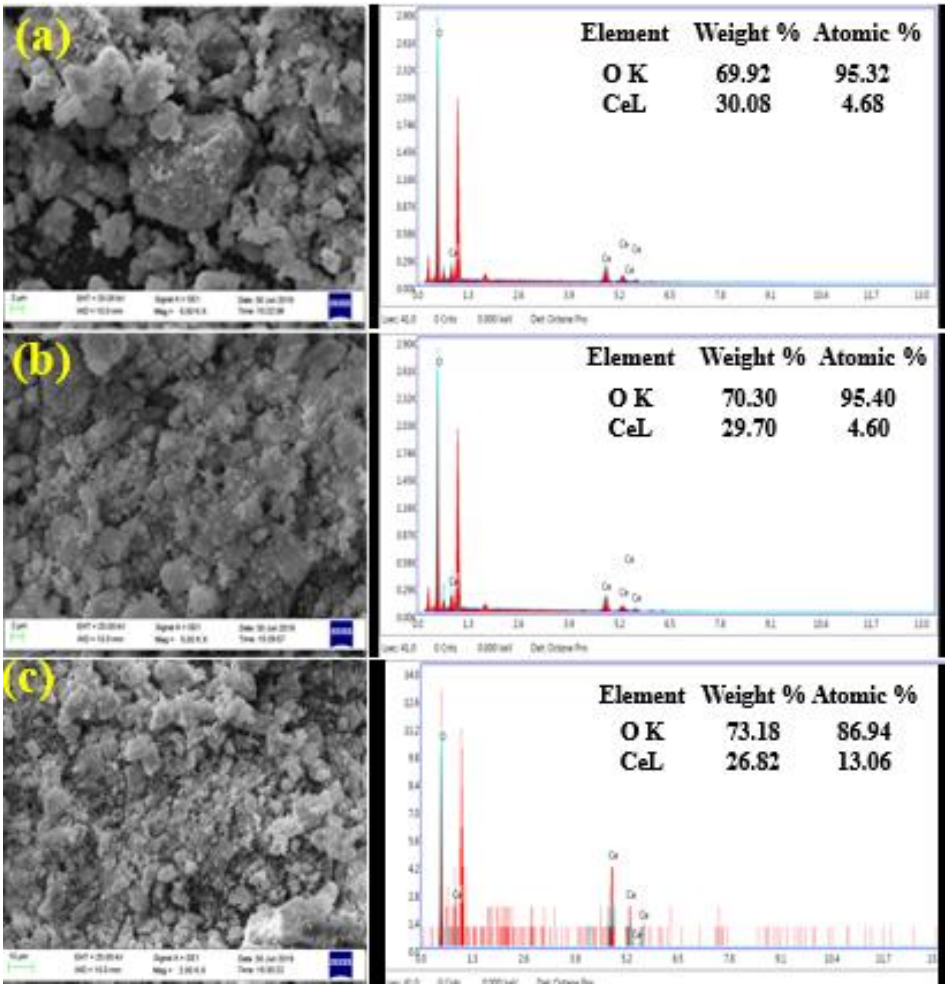

Fig. 4.8. SEM-EDX of the samples: (a) CeO_2-NR, (b) CeO_2-NC, and (c) CeO_2-NP

4.2.5. Scanning Electron Microscopy-Energy Dispersive X-ray Analysis (SEM-EDX)

The chemical composition of CeO_2 nanocrystals was anaylzed using scanning electron microscopy with energy-dispersive X-ray spectroscopy (SEM-EDX) and elemental mapping. SEM-EDX is a valuable technique that enables simultaneous imaging and elemental analysis of the sample. In **Fig. 4.8**, we observe the surface morphology of CeO_2, revealing that the particles exhibit irregular shapes and sizes in the CeO_2-NR, CeO_2-NC, and CeO_2-NP samples. The SEM images indicate that CeO_2-NC and CeO_2-NP nanocrystals possess smoother surfaces than CeO_2-NR. This observation is crucial because surface roughness increases the catalyst's surface area, providing additional chemical processes at reaction sites. It was validated using BET data that CeO_2-NR had a higher surface area than CeO_2-NR.

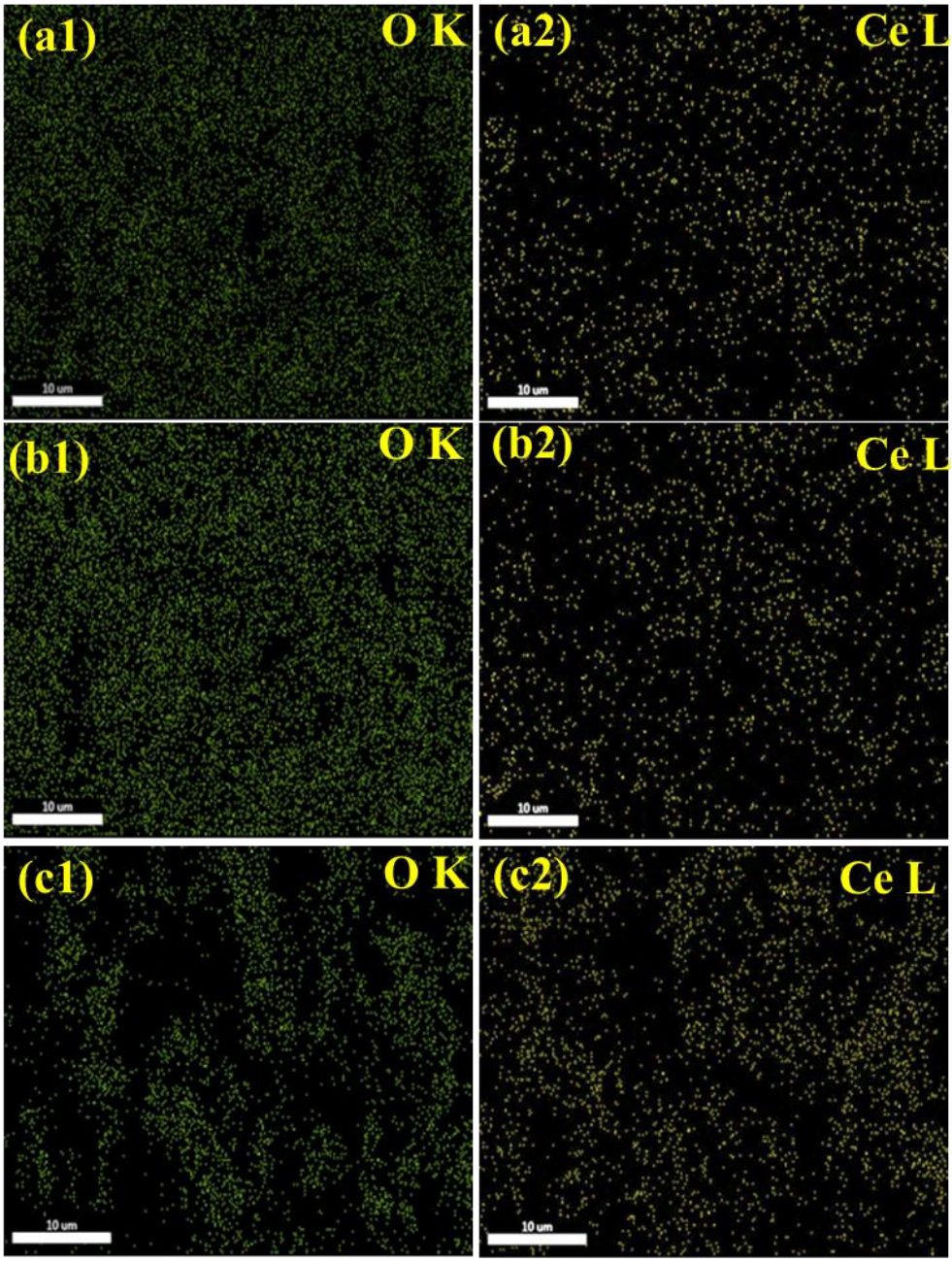

Fig. 4.9. Elemental mapping of the CeO_2-NR (a1, a2), CeO_2-NC (b1, b2), and CeO_2-NP (c1, c2)

EDX was employed to investigate the elemental composition of the synthesized samples. The results presented in **Fig. 4.8** confirmed the presence of the essential elements, namely Ce and O. The significant presence of Ce (%) and O (%) indicated the formation of CeO_2, highlighting these elements as the key components. For the EDX analysis, a small sample was used, assuming that the material exhibited a homogeneous composition. This assumption allowed for

the accurate representation of the elemental makeup of the entire sample based on the anaylzed portion.

To further validate the uniform distribution of elements in the synthesized materials, elemental mapping was conducted and depicted in **Fig. 4.9**. The elemental mapping results provided evidence that all elements necessary for CeO_2 were present in the samples and were evenly distributed throughout the material.

4.2.6. Raman Spectroscopy

Raman spectroscopy of ceria support was investigated to study the lattice vibration and defects in the support. **Fig. 4.10** presents the Raman spectra of ceria support with different morphologies. As shown in Fig. 10 (a), the peak centred around 465 cm^{-1} is associated with F_{2g} mode (Ce–O–Ce vibration) of CeO_2 fluorite. Additionally, weaker Raman bands were appeared at around 600 cm^{-1}, indicative of defect-induced mode (D) of ceria [10,11]. Generally, the integrated area ratio of D peak to F_{2g} peak (A_D/A_{F2g}) is related to oxygen vacancy concentration. **Fig. 4.11** shows the oxygen vacancy concentration for ceria supports and increased in the order: CeO_2-R (0.150) > CeO_2-P (0.0101) > CeO_2-C (0.009), showing that oxygen vacancy concentration varies with the morphologies

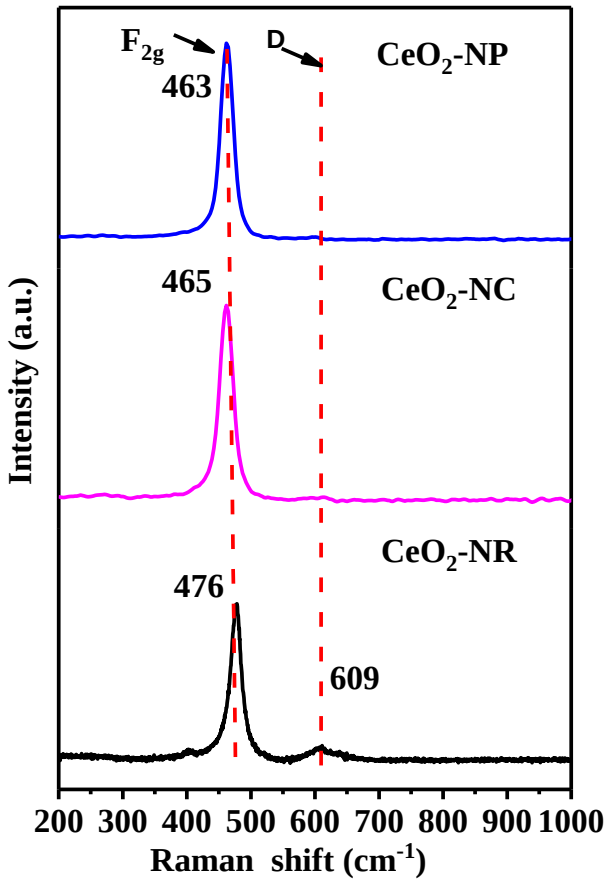

Fig. 4.10. Raman spectra of the catalysts

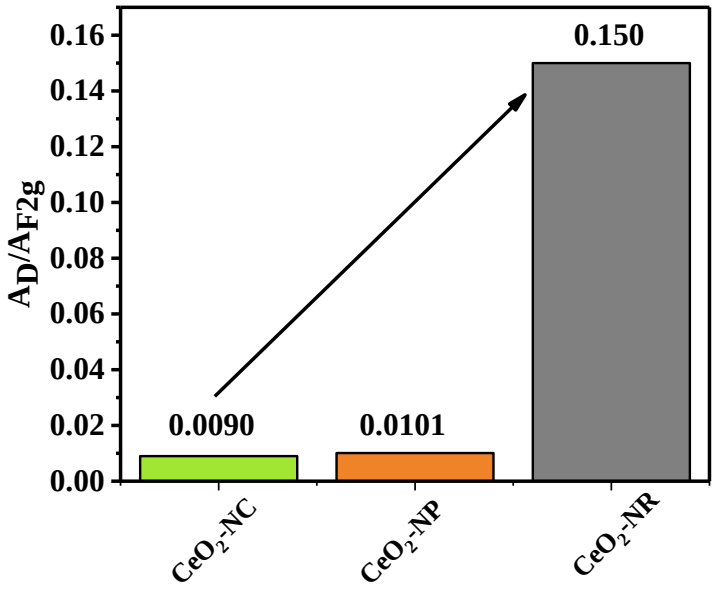

Fig. 4.11. Ratio of A_D/A_{F2g} of the different catalysts

4.2.7. Hydrogen-Temperature Programmed Reduction (H_2-TPR)

H_2-TPR experiments were conducted to determine the effect of CeO_2 morphology on the reducibility of the samples, which is shown in **Fig.4.12**. There is a reduction peak on CeO_2 catalysts at about 250–287 °C and a reduction peak at about 398-423 °C. The centres of the reduction peaks appear for CeO_2-NR at 287 and 409°C, for CeO_2-NC at 256 and 398°C, and for CeO_2-NP at 250 and 423°C. All three CeO_2 catalysts undergo reduction at low temperatures (250-287°C), but CeO_2-NR exhibits a greater reduction peak area than its two catalysts. The low-temperature reduction performance of CeO_2-NR is better than those of the other two catalysts. The peak at lower temperature is due to the reduction of surface oxygen and peak at higher temperature corresponds to the reduction of lattice oxygen of bulk CeO_2 ($Ce^{4+} \rightarrow Ce^{3+}$). [12,13] **Table 4.5** shows the amount of hydrogen consumed by the samples in the H_2-TPR experiments. In all these data, the CeO_2-NP showed the lowest hydrogen consumption while CeO_2-NR catalyst exhibited highest hydrogen consumption.

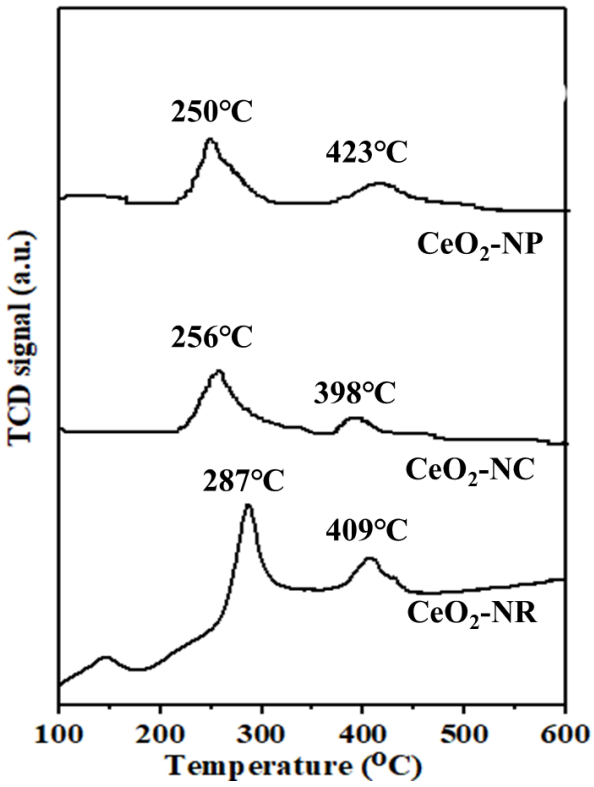

Fig. 4.12. H_2-TPR of CeO_2-NR, CeO_2-NC, and CeO_2-NP catalysts

Table 4.5. H_2-TPR data of catalysts

Sample	Reduction temperature (℃)		Hydrogen consumption ($mmol.gm^{-1}$)
	Lower	Higher	
CeO_2-NR	287	409	1.30
CeO_2-NC	256	398	1.21
CeO_2-NP	250	423	1.17

4.2.8. Catalytic Performance

4.2.8.1. Effects of temperature on CeO_2 morphologies for the NO reduction

Fig.4.13 illustrates how different CeO_2 catalysts perform in NH_3-SCR. As shown in **Fig. 4.13**, It has been demonstrated that catalyst morphologies affect the activity of NH_3-SCR. CeO_2-NR exhibits the highest performance (48% NO conversion) in NH_3-SCR, followed by CeO_2-NC (41%), and CeO_2-NP (35%) shows the lowest performance. The effect of reaction temperature on the NH_3-SCR process is observed. At temperatures below 250ºC, the NO conversion rate increases with rising reaction temperature. However, beyond 250ºC, the NO conversion rate starts to decline. This behaviour can be attributed to increased surface energy at lower temperatures, enhancing catalytic activity. Conversely, at higher temperatures, the oxidation of NH_3 to NO becomes more prevalent, resulting in decreased NH_3-SCR performance for the catalysts at those conditions. The N_2 selectivity followed the same path as the NO conversion for all the catalysts.

The large surface area and pore volume help enhance the SCR activity of CeO_2 catalysts. The CeO_2-NR catalyst exhibits superior performance compared to the other two catalysts, as the characterization data in **Table 4.2** supports. It has the highest surface area (22.751 m^2/g) and

pore volume (0.103 cm^3/g) among the three catalysts, resulting in more active surfaces and more effective reactant interactions. Furthermore, it contains more surface Ce^{3+} species (44%) and O_α (53%) than the other catalysts. The Raman characterizations in **Fig.4.10** show that the CeO_2-NR catalyst exhibits a greater diversity of surface-active oxygen species. The catalyst contains a higher concentration oxygen vacancy, crucial in promoting oxygen absorption and facilitating the formation of active surface oxygen species. This, in turn, accelerates the SCR reaction by promoting the conversion of NO to NO_2. Ce^{3+} species are essential for the SCR reaction as they contribute to redox reactions and enhance the catalyst's ability to adsorb and activate reactants like NH_3 and NO. All these parameters are responsible, which enhanced the CeO_2-NR catalyst performance.

Equation (4) was used to compute the turnover frequency (TOF) for each catalyst at three temperatures: 150, 200, 250, and 300℃, with the results reported in **Table 4.6.** The results showed that temperature, catalyst quantity, and H_2 consumption affected the TOF. CeO_2-NP had the lowest TOF (0.850 s^{-1}) at 350℃ among all catalysts. The TOF values are 1.023 and 0.921 s^{-1} for CeO_2-NR and CeO_2-NC. The highest TOF value will be the performance, and the results also confirm that CeO_2-NR has the highest NO activity and CeO_2-NP has the lowest, which follows the same TOF pattern of the catalysts.

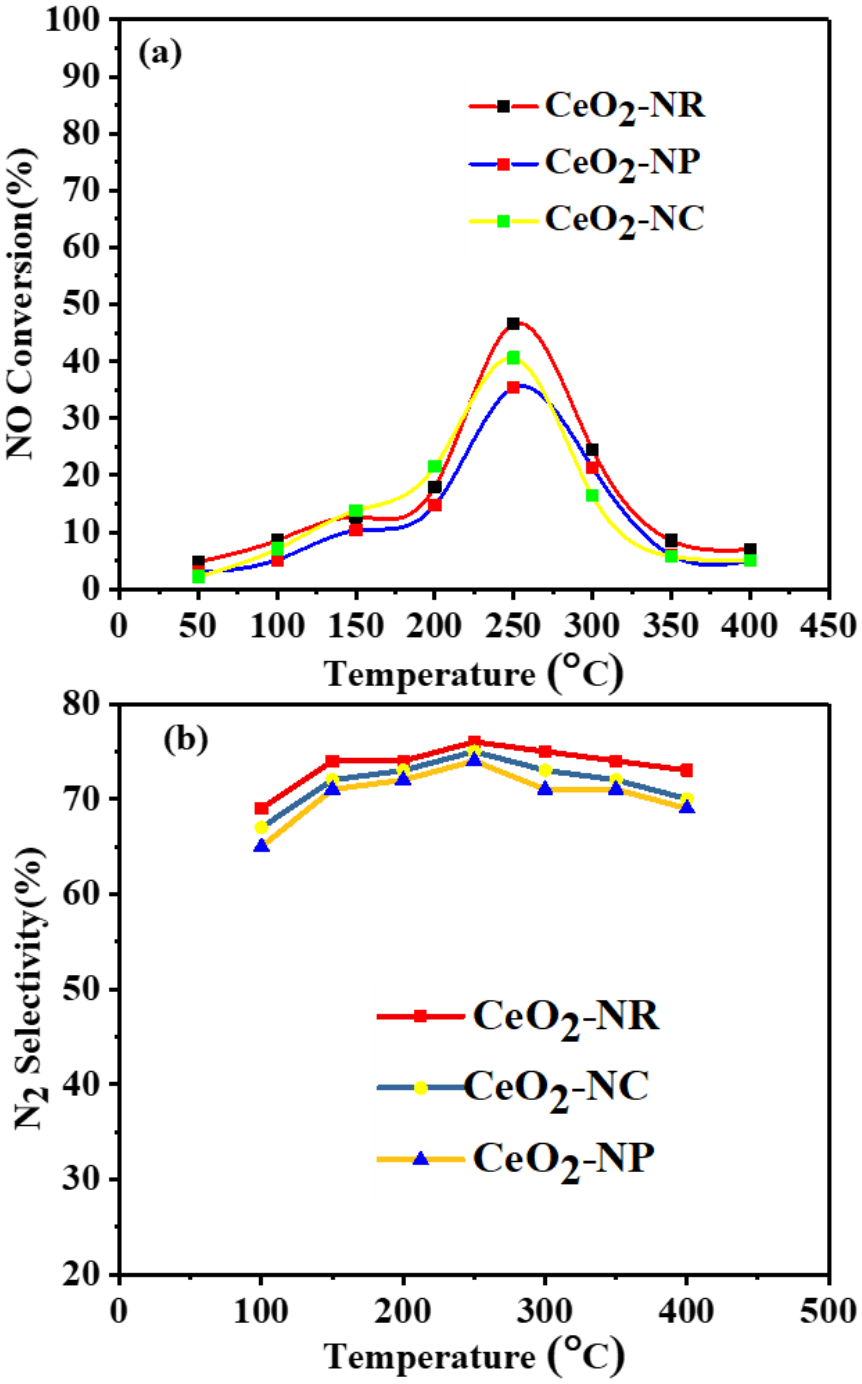

Fig. 4.13. (a) NO conversion, and (b) N_2 selectivity. Reaction conditions: 0.4 gm catalyst, temperature range 50 to 450°C, NO, NH_3 =1000 ppm, O_2=6 vol%, Ar balance, and GHSV =13,000 h^{-1}

Table 4.6. Turnover frequency (TOF) of the samples at different temperatures

Catalyst	TOF (s^{-1}) at 150°C	TOF (s^{-1}) at 200°C	TOF (s^{-1}) at 250°C	TOF (s^{-1}) at 300°C
CeO_2-NR	0.801	0.864	1.023	0.874
CeO_2-NC	0.862	0.872	0.921	0.857
CeO_2-NP	0.820	0.856	0.850	0.812

Fig.4.14 illustrates the intricate relationship between reaction rate and turnover frequency (TOF) with temperature. In **Fig.4.14(a)**, the reaction rate is low at a lower temperature of 150°C. However, as the temperature increased, the rate increased, giving a maximum rate at 250°C. This observable escalation in reaction rates up to 250°C suggests a positive correlation between temperature and the kinetics of the reaction. The surge in the reaction rates up to 250°C is attributed to the heightened generation of active sites. The abundance of active sites facilitates a more expeditious reaction progression, accelerating the rate. Beyond the critical temperature of 250°C, this trend reverses as the reaction rate initiates a gradual descent. This decline could indicate factors such as thermal degradation or deactivation of active sites at elevated temperatures.

Turning attention to **Fig.4.14(b)**, the focus shifts to the turnover frequency (TOF) in conjunction with temperature variations. The graph distinctly portrays an escalating trend in TOF as the temperature rises. Specifically, at 250°C, a notable surge in TOF indicates a concurrent activation of more active sites. This alignment between temperature and TOF underscores the pivotal role of temperature in influencing the availability and activation of active sites, crucial factors governing the catalytic efficacy in the examined reaction system.

These findings shed light on the intricate interplay between temperature, active site dynamics, and the resulting reaction kinetics.

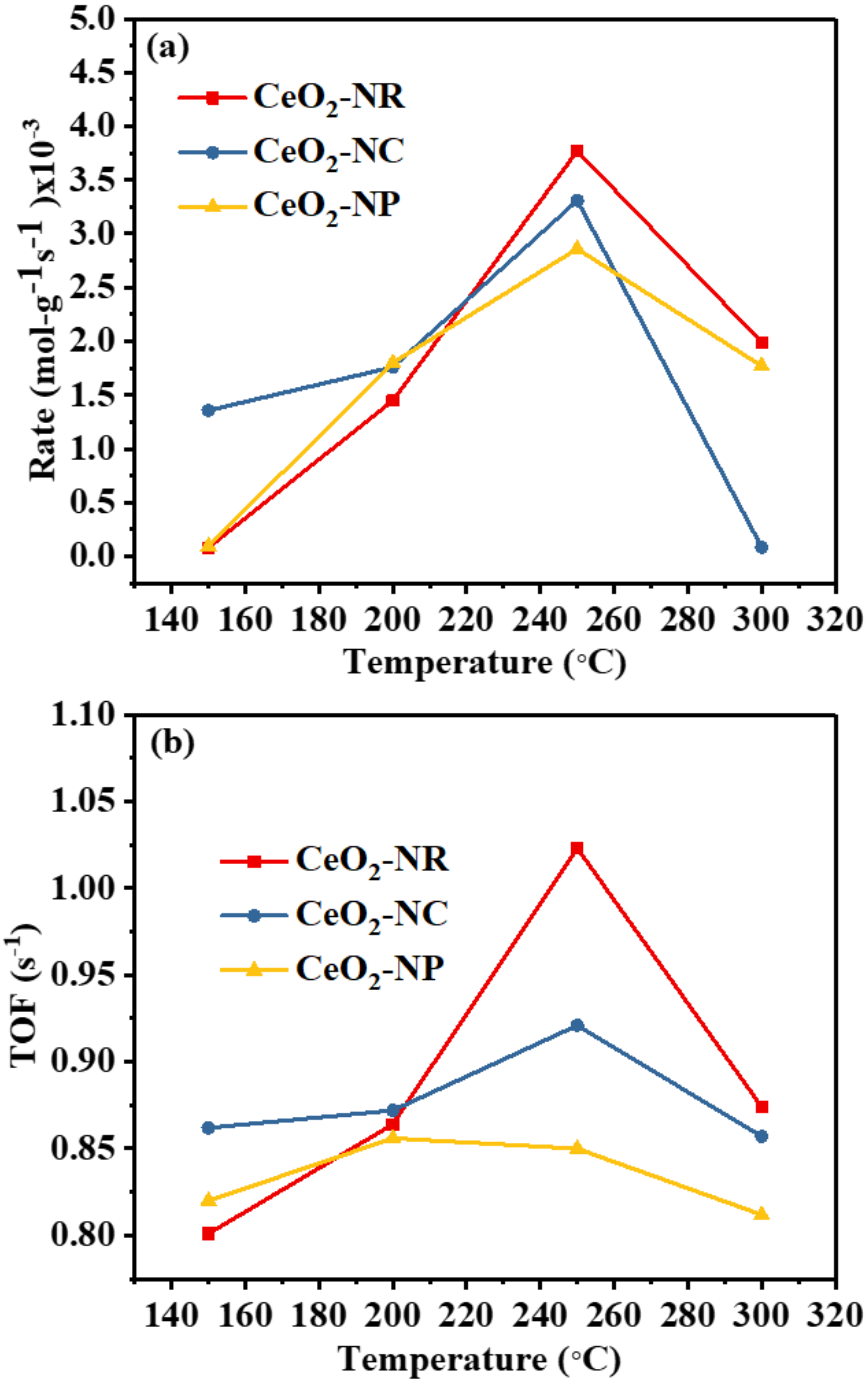

Fig. 4.14. Graphs between the (a) Reaction rate vs temperature, and (b) TOF vs temperature

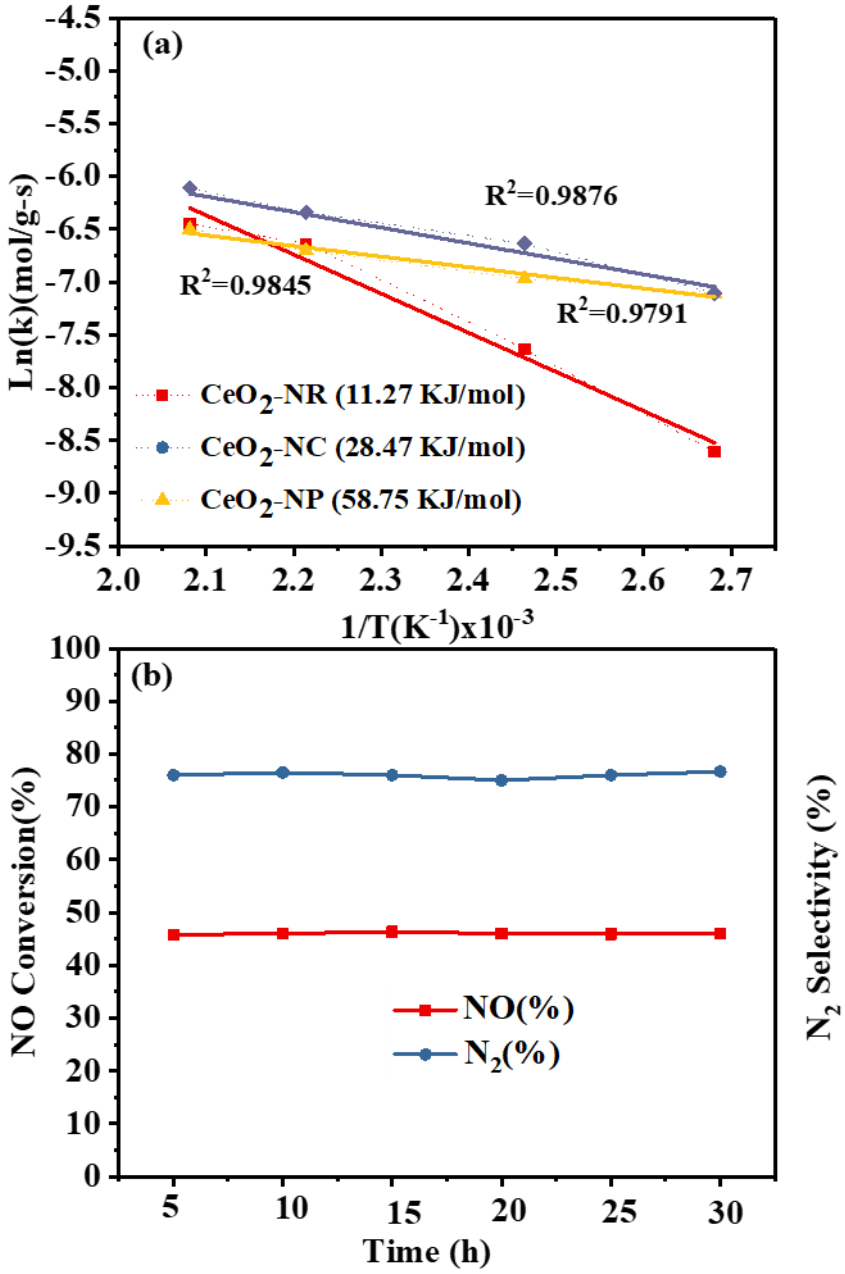

Fig. 4.15. (a) Activation energy of the catalysts, and (b) Catalyst stability test

Fig. 4.15(a) illustrates the Arrhenius plots for the NH_3-SCR reaction of each of the three catalysts. All three catalysts operate via the same NH_3-SCR mechanism to reduce NO, as indicated by their activation energies falling within a range of 11 to 59 KJ mol^{-1}, which aligns with previous research results [14,15]. Among the catalysts, the CeO_2-NR catalyst exhibits the

lowest activation energy of 11.27 KJ mol^{-1}, indicating that it requires less energy to facilitate the NH_3-SCR reaction and enhance NO conversion. On the other hand, the CeO_2-NP catalyst demonstrates the highest activation energy of 58.75 KJ mol^{-1}, implying that it demands relatively higher energy input to promote the NH_3-SCR process and achieve NO reduction. These activation energy values play a crucial role in understanding the catalytic performance of each catalyst and can explain the differences in their NH_3-SCR efficiency. The lower activation energy of CeO_2-NR suggests better catalytic activity, while the higher activation energy of CeO_2-NP implies comparatively lower catalytic efficiency for NO reduction through the NH_3-SCR mechanism.

4.2.8.2. Stability test of the catalyst

Fig. 4.15(b) shows the results of a stability assessment of the CeO_2-NR catalyst. The evaluation consisted of long-duration isothermal tests at 250°C under specific reaction gas conditions, including NO and NH_3 concentrations at 1000ppm, O_2 concentration at 6 vol%, and the remaining balance as Ar. The experiment was performed with a gas flow rate of 100 ml-min-1, corresponding to a gas hourly space velocity (GHSV) of 13,000 h^{-1} and a catalyst mass of 0.4 g. The CeO_2-NR catalyst demonstrates outstanding catalytic stability, as depicted by the NO conversion and N_2 selectivity data as a function of time. Throughout 24 h at 250 °C, the catalyst maintains NO conversion rates above 46±1% and N_2 selectivity above 76±1%. This high and sustained catalytic performance underscores the excellent stability of the CeO_2-NR catalyst, a crucial attribute for its practical application in real-world scenarios.

4.2.8.3. Characterization of spent catalysts

The XRD pattern of all spent catalysts is shown in **Fig.4.16**. The XRD pattern revealed an insignificant effect on the diffraction pattern, however an increase in sharpness in peaks was observed. There is also an increase in the crystal size of catalysts as shown in **Table 4.7**.

TEM images of spent catalysts are shown in **Fig.4.17**. Comparing **Fig.4.17** with Fig. **4.7**, the TEM images exhibited the same morphology, which means the effects of high temperature didn′t affect the catalysts′ morphology properties.

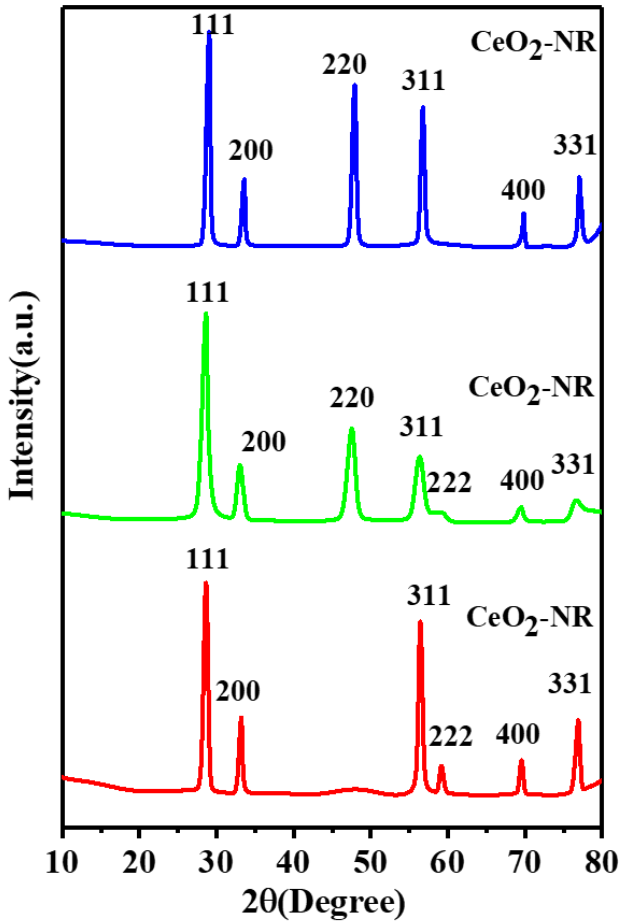

Fig. 4.16. XRD of spent CeO_2-NP, CeO_2-NC, and CeO_2-NR catalysts

Table 4.7. Average crystal size and particle size of the spent catalysts

Catalyst	**Average crystal size (nm)**	**Average particle size (nm)**
CeO_2-NP	13.85	39
CeO_2-NC	14.98	75
CeO_2-NR	15.34	46

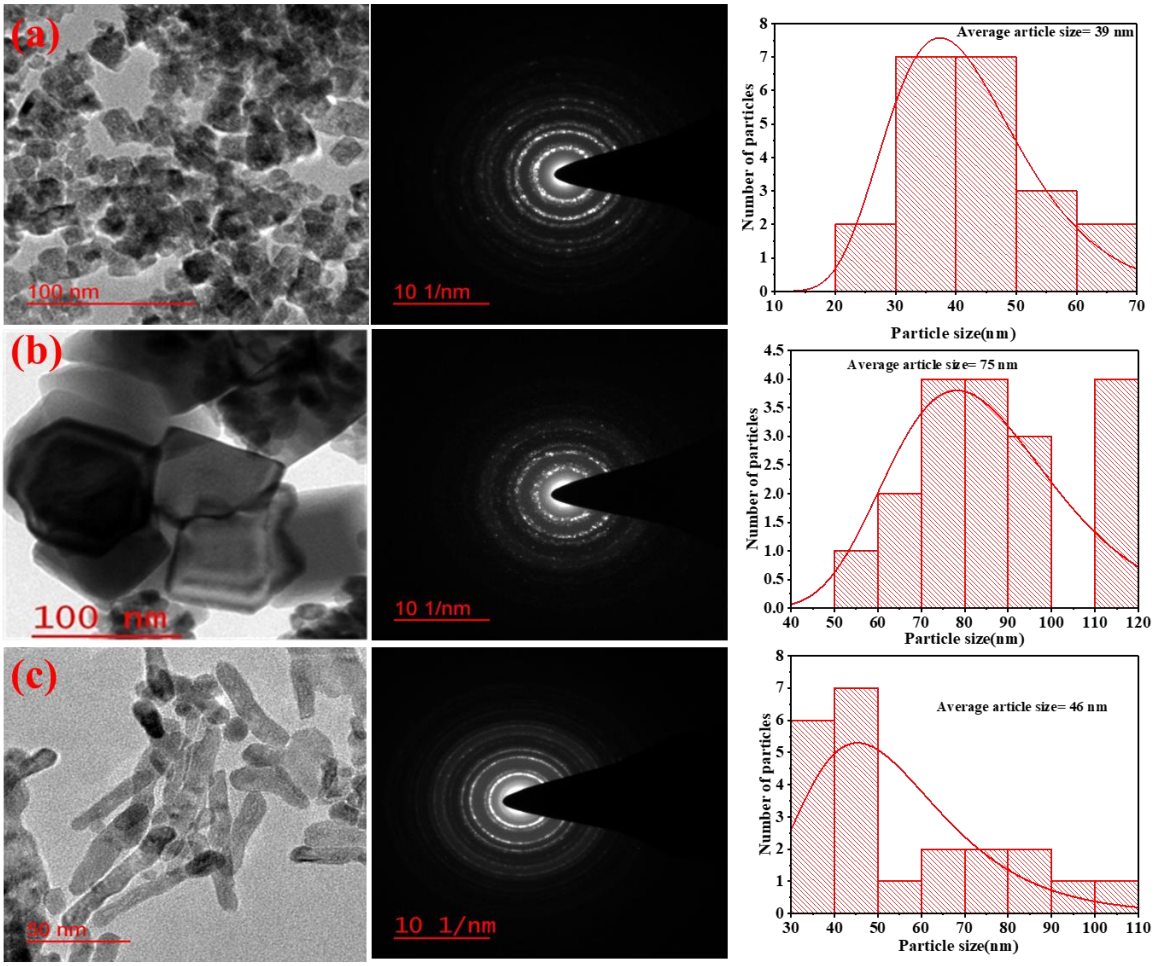

Fig. 4.17.TEM images of (a) spent CeO_2-NP, (b) spent CeO_2-NC, and (c) spent CeO_2-NR catalysts

4.3. Conclusions

In summary, the hydrothermal approach successfully synthesized CeO_2 catalysts with different morphologies. These catalysts were characterized through the BET, XRD, XPS, SEM-EDX, TEM, and Raman spectrograph. Among them, the CeO_2-NR catalyst demonstrated remarkable performance, achieving a NO conversion efficiency of 45% and N_2 selectivity of over 70% across a wide temperature range of 50-450℃. Several key factors contribute to the outstanding performance of the CeO_2-NR catalyst: high specific surface area and pore volume, higher oxygen vacancies, and Ce^{3+} species.

References

1. Zhan, S., Zhang, H., Zhang, Y., Shi, Q., Li, Y. and Li, X., 2017. Efficient NH_3-SCR removal of NO_x with highly ordered mesoporous WO_3 (χ)-CeO_2 at low temperatures. *Applied Catalysis B: Environmental*, *203*, pp.199-209.
2. Cao, J., Rohani, S., Liu, W., Liu, H., Lu, Z., Wu, H., Jiang, L., Kong, M., Liu, Q. and Yao, X., 2022. Influence of phosphorus on the NH_3-SCR performance of CeO_2-TiO_2 catalyst for NO_x removal from co-incineration flue gas of domestic waste and municipal sludge. *Journal of Colloid and Interface Science*, *610*, pp.463-473.
3. Tan, W., Wang, J., Cai, Y., Li, L., Xie, S., Gao, F., Liu, F. and Dong, L., 2022. Molybdenum oxide as an efficient promoter to enhance the NH_3-SCR performance of CeO_2-SiO_2 catalyst for NO_x removal. *Catalysis Today*, *397*, pp.475-483.
4. Zhou, Y., Ren, S., Yang, J., Liu, W., Su, Z., Chen, Z., Wang, M. and Chen, L., 2021. NH_3 treatment of CeO_2 nanorods catalyst for improving NH_3-SCR of NO. *Journal of the Energy Institute*, *98*, pp.199-205.
5. Shi, Y., Tan, S., Wang, X., Li, M., Li, S. and Li, W., 2016. Regeneration of Sulphur-poisoned CeO_2 catalyst for NH_3-SCR of NO_x. *Catalysis Communications*, *86*, pp.67-71.
6. Sun, X., Guo, R.T., Liu, S.W., Liu, J., Pan, W.G., Shi, X., Qin, H., Wang, Z.Y., Qiu, Z.Z. and Liu, X.Y., 2018. The promoted performance of CeO_2 catalyst for NH_3-SCR reaction by NH_3 treatment. *Applied Surface Science*, *462*, pp.187-193.
7. Yao, X., Wang, Z., Yu, S., Yang, F. and Dong, L., 2017. Acid pretreatment effect on the physicochemical property and catalytic performance of CeO_2 for NH_3-SCR. *Applied Catalysis A: General*, *542*, pp.282-288.
8. Guo, Q., Jing, W., Hou, Y., Huang, Z., Ma, G., Han, X. and Sun, D., 2015. On the nature of oxygen groups for NH_3-SCR of NO over carbon at low temperatures. *Chemical Engineering Journal*, *270*, pp.41-49.

9. Tan, W., Wang, C., Yu, S., Li, Y., Xie, S., Gao, F., Dong, L. and Liu, F., 2021. Revealing the effect of paired redox-acid sites on metal oxide catalysts for efficient NO_x removal by NH_3-SCR. *Journal of Hazardous Materials*, *416*, p.125826.
10. Jayakumar, G., Albert Irudayaraj, A. and Dhayal Raj, A., 2019. A comprehensive investigation on the properties of nanostructured cerium oxide. *Optical and Quantum Electronics*, *51*(9), p.312.
11. Zhang, Z., Wang, Y., Wang, M., Lü, J., Li, L., Zhang, Z., Li, M., Jiang, J. and Wang, F., 2015. An investigation of the effects of CeO_2 crystal planes on the aerobic oxidative synthesis of imines from alcohols and amines. *Chinese journal of catalysis*, *36*(9), pp.1623-1630.
12. He, J., Zhang, H., Wang, W., Yao, P., Jiao, Y., Wang, J. and Chen, Y., 2021. Soot combustion over CeO_2 catalyst: the influence of biodiesel impurities (Na, K, Ca, P) on surface chemical properties. *Environmental Science and Pollution Research*, *28*, pp.26018-26029.
13. Li, L., Jiang, B., Tang, D., Zheng, Z. and Zhao, C., 2018. Hydrogen production from chemical looping reforming of ethanol using Ni/CeO_2 nanorod oxygen carrier. *Catalysts*, *8*(7), p.257.
14. Wang, H., Wang, L., Luo, Q., Zhang, J., Wang, C., Ge, X., Zhang, W. and Xiao, F.S., 2022. Two-dimensional manganese oxide on ceria for the catalytic partial oxidation of hydrocarbons. *Chem. Synth*, *2*(1), p.2.
15. Gan, L., Li, K., Xiong, S., Zhang, Y., Chen, J., Peng, Y. and Li, J., 2018. MnO_x-CeO_2 catalysts for effective NO_x reduction in the presence of chlorobenzene. *Catalysis Communications*, *117*, pp.1-4.